PHYSICAL REVIEW A **103**, 063507 (2021)

Photonic non-Bloch quadrupole topological insulators in coupled ring resonators

Zekun Lin,[1,2] Lu Ding,[2] Shuyue Chen,[2] Shan Li,[2] Shaolin Ke,[1,*] Xun Li,[3] and Bing Wang[2,†]
[1] *Hubei Key Laboratory of Optical Information and Pattern Recognition, Wuhan Institute of Technology, Wuhan, 430205, China*
[2] *Wuhan National Laboratory for Optoelectronics, School of Physics, Huazhong University of Science and Technology, Wuhan, 430074, China*
[3] *Department of Electrical and Computer Engineering, McMaster University, Hamilton, Ontario L8S 4K2, Canada*

(Received 5 April 2021; revised 21 May 2021; accepted 2 June 2021; published 14 June 2021)

We investigate the second-order topological phases in a two-dimensional ring resonator array with each plaquette occupied by π gauge flux and imaginary gauge field. The real and imaginary gauge fields are induced by shifting the displacement and integrating gain or loss into the two half perimeters of the auxiliary rings. The system supports topological corner modes with their emergence being determined by the non-Bloch topological invariant due to skin effects. The bulk modes, exhibiting second-order skin effects in both trivial and nontrivial phases, are accumulated at opposite corners depending on whether clockwise or counterclockwise modes are excited. By introducing an interface with different imaginary gauge fields, we show the bulk modes exist at the interface while the topological corner modes are localized at the physical corners. Furthermore, the skin effects are also presented in the passive ring resonators. The study may find applications in lasers and broadband light trapping.

DOI: 10.1103/PhysRevA.103.063507

I. INTRODUCTION

Topological photonics promises novel design of integrated photonic circuits that minimize fabrication imperfections in aid of topological boundary states [1–11]. Various topological phases have been discovered in photonic lattices under the interplay of external magnetic field [2], spin-orbit interaction [11], and valley degree of freedom [12]. Ring resonators are widely utilized to demonstrate topological lattice phenomena [13] since the effective gauge fields for photons are conveniently introduced by geometrical design via auxiliary rings [14], dynamical modulation of refractive index [15,16], or taking account of backscattering between clockwise and counterclockwise modes [17]. Therefore, a wide variety of ring-resonator based topological models are proposed in one, two, and synthetic higher dimensions, such as the photonic analogy of quantum Hall effects [14], anomalous Floquet topological phases [18,19], and Weyl points [20]. Recently, the concept of high-order topological phases was suggested to generalize the bulk-boundary correspondence which relates robust boundary modes to bulk topological invariants [21–23]. A high-order topological insulator supports topological modes with at least two dimensions lower than that of the system itself. For example, a two-dimensional second-order topological insulator hosts zero-dimensional modes at its corners, in contrast to the first-order insulator with one-dimensional edge modes. The existence of these corner modes is guaranteed by a quantized bulk quadrupole moment instead of dipole momentum, giving rise to the quadrupole topological insulators [24,25]. The corner modes are robust and independent of system termination and are experimentally observed in silicon-based ring resonators [26].

Recent research interest of topological phases has been extended to non-Hermitian systems [27–34]. The skin effects were proposed in non-Hermitian systems as a result of asymmetric couplings, with mode accumulation at the boundaries, which dramatically breaks the conventional bulk-boundary correspondence [35]. The topological invariants defined in Brillouin zone are not essential to predict the existence of robust edge modes under open boundary conditions, stimulating many theoretical investigations [35–44]. The principle is revised by utilizing non-Bloch theory via including an imaginary gauge transformation [27]. The skin effects and non-Bloch theory are experimentally observed in quantum walks [45] and synthetic mesh lattices [46], which are further investigated in two-dimensional systems with high-order topology [47–51]. The interplay between non-Hermiticity and high-order topology leads to novel effects. In addition to zero-energy topological corner modes, a two-dimensional system also hosts second-order skin effects with bulk modes accumulated at its corners [47]. However, it is difficult to realize the non-Bloch quadrupole insulator as the model requires both negative and non-Hermitian asymmetric coupling.

In this work, we construct such topological insulators by utilizing evanescently coupled optical ring resonators where adjacent site rings are indirectly connected via link rings. The negative coupling can be induced by shifting the link rings to arouse real gauge fields [14], while the non-Hermitian asymmetric coupling is accomplished by inserting asymmetric gain and loss into link rings to effectively generate imaginary gauge fields [52–58]. The magnitudes of coupling and the imaginary gauge field can be flexibly tuned by the spatial gap distance and the amount of gain and

---

[*] keshaolin@wit.edu.cn
[†] wangbing@hust.edu.cn

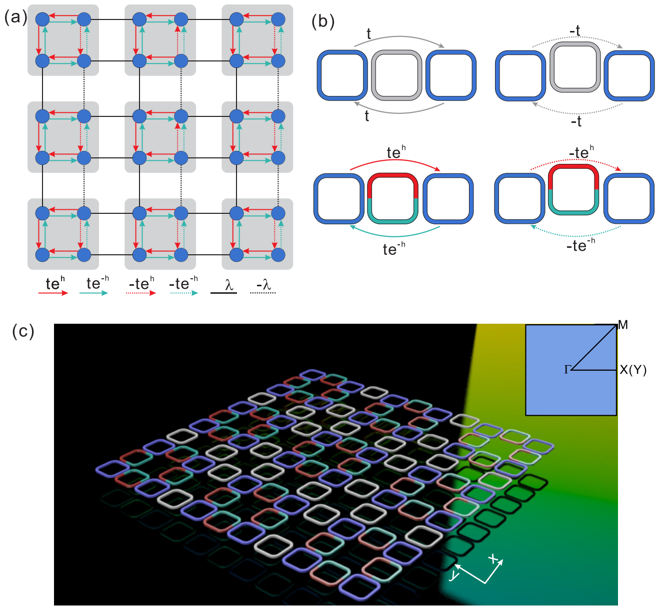

FIG. 1. Schematic of non-Bloch quadrupole topological insulator. (a) Tight-binding model. The black solid lines represent the symmetric intercell coupling, and the red and green arrows indicate the asymmetric intracell coupling. The dashed lines denote the negative coupling. (b) Different kinds of couplings accomplished in ring resonators by engineering the link rings. (c) The geometry of proposed ring resonator arrays. The blue represents site rings, while the gray, green, and red denote the link rings. The inset plots the first Brillouin zone.

loss, respectively. Subsequently, the topological phases can be manifested as desired. There are two important issues to understand, the existence of the skin modes and topological corner modes, which is determined by the generalized Brillouin zone and non-Bloch winding number. We show the location of skin modes is dependent on the excitation direction of clockwise and counterclockwise modes. In addition, as the origins of corner and skin modes are different, we show they exhibit distinct behaviors at the interface between two structures with different imaginary gauge field or topologies. We also discuss a passive system and derive the related tight-binding Hamiltonian using transfer matrix method.

II. THEORETICAL MODEL

The tight-binding model of the proposed non-Hermitian insulator is schematically shown in Fig. 1(a). The system is arranged in a square lattice with each unit cell comprising four sites, where the intracell coupling is asymmetric denoted by $te^{\pm h}$ and the intercell coupling is symmetric represented by λ. Each unit cell also contains a negative coupling, which effectively introduces a π gauge flux. The model is an extension of Hermitian quadrupole insulator with asymmetric intracell coupling qualified by the imaginary gauge field ih. The Bloch Hamiltonian can be written in an off-diagonal form as

$$H=\begin{pmatrix} & & te^{-h}+\lambda e^{ik_x} & -te^{-h}-\lambda e^{ik_y}\\ & & te^{h}+\lambda e^{-ik_y} & te^{h}+\lambda e^{-ik_x}\\ te^{h}+\lambda e^{-ik_x} & te^{-h}+\lambda e^{ik_y} & & \\ -te^{h}-\lambda e^{-ik_y} & te^{-h}+\lambda e^{ik_x} & & \end{pmatrix}, \quad (1)$$

where k_x and k_y represent the Bloch momentum along x and y directions, respectively. For the Hermitian quadrupole topological insulator, the system hosts midgap second-order topological modes located at each of four physical corners when the intercell coupling is stronger than the intracell coupling, that is, $\lambda > t$. The topological modes are protected against certain disorders, which is attributed to two noncommuting reflection symmetries $M_x = \tau_x\sigma_z$ and $M_y = \tau_x\sigma_x$ and fourfold rotational symmetry $C_4 = [(\tau_x - i\tau_y)\sigma_0 - (\tau_x + i\tau_y)(i\sigma_y)]/2$ with σ and τ denoting Pauli matrices. In addition, the system obeys sublattice symmetry $S = \tau_z$, pinging the second-order topological modes to zero energy. These modes are related to the bulk quadrupole momentum rather than a dipole one. Its topological property can be characterized by the nested Wannier bands and the topological quadrupole momentum [21]. When imaginary gauge fields are introduced, the mirror and C_4 symmetries are broken. Instead, the system preserves sublattice symmetry and mirror-rotation symmetry $M_{xy} = C_4M_y$ [47].

Different types of coupling can be realized between two site rings connected via a link ring, as shown in Fig. 1(b). The resonant frequency of link ring varies from that of site ring by setting an extra length, which allows one to manipulate the phase and magnitude of the coupling. Such a scheme directly introduces an evanescent coupling t, whose strength is controlled via the gap distance between two rings. By vertically shifting the link ring, light that couples from right to left and left to right experiences different path lengths, yielding a direction-dependent phase φ which is π in our system constructing a negative coupling $-t$. Similarly, by integrating the same amount of gain and loss into the two semicircles of link ring, direction-dependent amplification or dissipation is induced, giving rise to non-Hermitian asymmetric coupling $te^{\pm h}$ with imaginary gauge field [51]. Furthermore, the coupling becomes $-te^{\pm h}$ if we simultaneously shift the link ring and incorporate gain and loss. The geometry of proposed ring resonator arrays is shown in Fig. 1(c), where the insert represents the first Brillouin zone.

The system supports four energy bands, which are doubly degenerate due to the existence of π flux [21]. The periodic eigenvalues are derived as

$$E = \pm\sqrt{\lambda t(e^{h+ik_x} + e^{-h-ik_x} + e^{h-ik_y} + e^{-h+ik_y}) + 2(\lambda^2 + t^2)}. \quad (2)$$

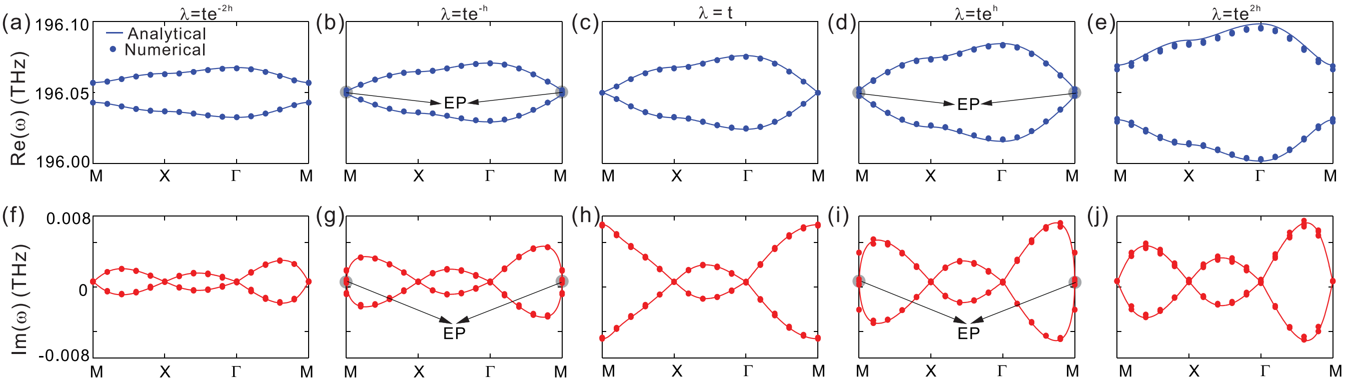

FIG. 2. Band structures versus various intracell couplings. (a–e) The real part of band structures for $g_\lambda = 0.293, 0.322, 0.350, 0.379, 0.408$ μm. (f–j) The imaginary part corresponding to (a)–(e). In all cases, the intercell gap and gain-loss coefficient are fixed at $g_t = 0.350\,\mu$m and $\gamma = 0.01$, respectively.

In Fig. 2 we plot the real and imaginary parts of band structures for different couplings. When $\lambda = te^{-h}$ [Figs. 2(b) and 2(g)] and $\lambda = te^{h}$ [Figs. 2(d) and 2(i)], the real and imaginary parts of band structures coalesce at M point ($k_x = \pi, k_y = \pi$). Considering the twofold degeneracy of band structures, these points are the fourth-order exceptional point. As $\lambda < te^{-h}$ [Figs. 2(a) and 2(f)] and $\lambda > te^{h}$ [Figs. 2(e) and 2(j)], the real part is gaped while $\mathrm{Im}(\omega)$ is gapless. In contrast, $\mathrm{Re}(\omega)$ is closed and $\mathrm{Im}(\omega)$ is open in the range $te^{-h} < \lambda < te^{h}$ [Figs. 2(c) and 2(h)]. The closing points imply topological transition under periodic boundary condition. We also perform full wave simulations based on Comsol. The refractive index of core and cladding is $n = 3$ and $n_{\mathrm{air}} = 1$, respectively. The waveguide whose core width is fixed at $w = 0.27\,\mu$m supports only a single TE-polarized mode with effective refractive index $n_{\mathrm{eff}} = 2.39$ at frequency $\omega_0 = 196.05$ THz. The vertical and horizontal lengths of site rings are $L_1 = L_2 = 8\,\mu$m with fillet radius $r = 3\,\mu$m. The extra length of link rings is set to be $\Delta L = \pi/(n_{\mathrm{eff}}k_0)$ to fulfill the antiresonant condition. The resonant frequency of the site ring is figured to be $\omega_0 = (196.05 + 6i \times 10^{-4})$ THz with a small imaginary part induced by radiation loss. The intracell gap is fixed at $g_t = 0.35\,\mu$m, while the intercell gap g_λ is altered to tune the coupling. The magnitude of the imaginary gauge field increases with the augment of gain-loss coefficient γ, which is the imaginary part of the refractive index of gain-loss link rings. We select $\gamma = 0.01$ unless otherwise specified. Under these parameters, we have $t = 8.9$ GHz and $h = 0.51$. The intercell couplings in Fig. 2 are $\lambda = 3.2$, 5.4, 8.9, 14.8, and 24.5 GHz, respectively. The simulations plotted (dots) in Fig. 2 agree well with the theoretical results (lines).

The open-boundary spectra dramatically deviate from that of periodic system because of the skin effect. The open system whose eigenvalues are real numbers (neglect the uniform radiation loss) exhibits distinct phase transition points. In Fig. 3(a) we plot the eigenvalues as a function of intracell coupling. We observe the zero-energy corner modes in the range $-1 < t/\lambda < 1$. In addition, the system keeps the realness of its spectrum irrespective of its non-Hermitian nature because the open-boundary Hamiltonian exactly resembles the Hermitian quadrupole counterparts by taking a gauge transformation [47,57]. Therefore, the open-boundary eigenvalues remain unchanged with different h. On the other hand, the bulk modes will be accumulated at the structure corners as $h \neq 0$, referred to as second-order skin effects. Figures 3(b) and 3(c) plot intensity distributions of bulk eigenmodes at two typical frequencies. For Hermitian cases, the fields are distributed throughout the structure. For non-Hermitian cases, the eigenmodes are mainly confined at lower-left and top-right corners and decay exponentially with distance from the two corners.

Generally, the transition from periodic boundary to open boundary is considered as perturbation. Therefore, the topological invariant calculated by the periodic bulk modes is able to predict the existence of robust boundary modes according to the bulk-boundary correspondence. However, the

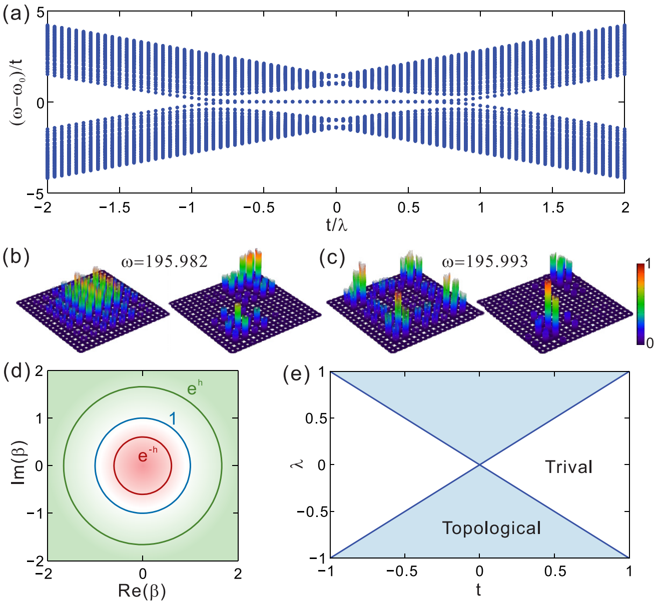

FIG. 3. The skin effects and the non-Bloch bulk-boundary correspondence. (a) The open-boundary spectrum as a function of the intracell coupling t. (b, c) The two typical intensity ($|\mathbf{E}|^2$) distributions of bulk modes. In both cases, the left and right panels are for $\gamma = 0$ and $\gamma = 0.01$, respectively. The gap distance for (b)–(c) is fixed at $g_t = 0.35$ and $g_\lambda = 0.26\,\mu$m. (d) The generalized Brillouin zone. (e) The topological phase diagram with $h = 0.51$, which is used in the following simulation.

non-Hermitian skin effects violate the framework and require essential revisions of this guiding principle. The non-Bloch-wave character of bulk modes should be taken into account when calculating the topological invariant on a generalized Brillouin zone. Our system has mirror-rotation symmetry, and thus the Hamiltonian can be expressed on a block-diagonal form with $k_x = k_y = k$ [47],

$$U^{-1}H(k,k)U = \begin{pmatrix} H_+(k) & \\ & H_-(k) \end{pmatrix}, \tag{3}$$

where U is a unitary transformation matrix. The generalized Brillouin zone C_β is obtained by replacing the Bloch phase factor $e^{ik} \to \beta$ in $H_\pm$ and calculating [59]

$$\det\,[H_\pm(\beta) - E] = 0. \tag{4}$$

The above equation forms the algebraic equation for β, which is derived as

$$2t\lambda e^h \beta^2 + (2t^2 + 2\lambda^2 - E^2)\beta + 2t\lambda e^{-h} = 0. \tag{5}$$

As $t = 0$ or $\lambda = 0$, the energy is $E^2 = 2\lambda^2$ or $E^2 = 2t^2$. Then the coefficients before β vanish. Thus, we could not get the GBZ in this case. As $t \neq 0$ and $\lambda \neq 0$, we have

$$\beta_1\beta_2 = e^{-2h}. \tag{6}$$

The GBZ is the trajectory of β_1 and β_2 on the complex plane by enforcing $|\beta_1|$ and $|\beta_2|$ to satisfy the boundary condition, which leads to

$$|\beta_1| = |\beta_2| = e^{-h} = r, \tag{7}$$

with r being the radius of the generalized Brillouin zone of $H_+(\beta)$, forming a circle with radius e^h on the complex plane. Thereby we can get the C_β of $H_-(\beta)$ in the same way, which is identical to that of $H_+(\beta)$. There are degenerate clockwise and counterclockwise modes in ring resonators. If the clockwise modes experience a positive imaginary gauge field, the counterclockwise ones will undergo a negative h since the traveling path in the link ring is reversed. The generalized Brillouin zone is plotted in Fig. 3(d) with the radius $e^{-h}(e^h)$ within (outside) the unit circle. Any derivation from the unit circle yields skin effects. Especially, the majority of modes are accumulated at the lower-left (upper-right) corner with the decay length $L_{\text{skin}} = 1/h$ as C_β within (outside) the unit circle. The total winding number can be calculated by [47]

$$w = w_+ - w_-, \tag{8}$$

with the non-Bloch winding number given by

$$w_\pm = \oint_{BZ} \frac{dk}{4\pi i} \mathrm{Tr}\left[S'\tilde{H}_\pm^{-1}(\beta)\frac{d\tilde{H}_\pm(\beta)}{dk}\right], \tag{9}$$

with $\tilde{H}_\pm$ fulfilling

$$\frac{\tilde{H}_\pm}{\sqrt{2}} = \left(te^{-h} + \lambda\beta_0 e^{ik}\right)\sigma_\mp + \left(te^h + \frac{\lambda}{\beta_0}e^{-ik}\right)\sigma_\pm, \tag{10}$$

where $\sigma_\pm = (\sigma_x \pm i\sigma_y)/2$. Figure 3(e) shows the phase diagram of the winding number as a function of couplings t and λ where the imaginary gauge field is chosen as $h = 0.51$ used in the following simulation. The total winding number is $w = -2$ as $t < \lambda$ and $w = 0$ as $t > \lambda$. We also compared the phase diagram for other h, which keeps unchanged and is not affected by the magnitude of imaginary gauge field.

III. EXCITATION OF TOPOLOGICAL AND SKIN MODES

The remarkable feature of non-Hermitian quadrupole topological insulators is the coexistence of corner modes and skin modes. Our 2D system supports three different types of modes: second-order topological modes, second-order skin modes, and hybrid skin-topological modes [60,61]. The topological modes have zero energy, which is induced by the second-order topology of nontrivial bulk determined by the relative coupling strength. The second-order skin modes, corresponding to the bulk modes in Hermitian cases, experience skin effects in both the x and y directions and thus are located at the physical corners affected by the imaginary gauge field. Furthermore, some modes undergo a skin effect along one direction and topological localization along the other direction, resulting in hybrid skin-topological modes. In our systems with the system size $L \times L$, the total number of second-order skin modes is $\mathcal{O}(L^2)$, while the number of hybrid skin-topological modes is $\mathcal{O}(L)$. In contrast, the number of topological modes is independent of system size, which is $\mathcal{O}(1)$. These three kinds of mode can be excited by coupling external waveguides to the arrays. Figure 4(a) illustrates the tight-binding schematic of ring resonator with 10 × 10 sites as $t/\lambda \approx 0.2$. The corresponding eigenfrequencies are plotted in Fig. 4(b). There are eight second-order topological modes in the bandgap with frequency equal to that of the separate individual site ring. We place two external waveguides at right termination labeled A and B, which are independently utilized to stimulate the three different types of modes. We first consider the clockwise modes as light is injected from the upper port of the two couplers. The absorption spectra are shown in Fig. 4(c), where the solid lines and the dotted lines with filling areas represent the Hermitian and non-Hermitian cases, respectively. For corner excitation, the narrow absorption peaks appear around $\omega_0 = 196.05$ THz as the topological modes are excited. For excitation from coupler A, we see prominent absorption peaks in two ranges, $196 < \omega < 196.02$ THz and $196.09 < \omega < 196.11$ THz, corresponding to hybrid skin-topological modes. In addition, some small peaks are also observed in the range $\omega < 196$ THz and $\omega > 196.11$ THz, which originate from the second-order skin modes. This is because the second-order skin modes have little energy distributed in the boundary rings, which makes it difficult to excite them. In these frequencies, the system exhibits some amplification for non-Hermitian cases. To gain insight into skin effects, we plot spatial intensity profiles at three typical resonant peaks marked by the dashed lines. The topological modes are remarkably localized at the corner resonator near the injected coupler for both $\gamma = 0$ and 0.01, indicating the topological modes are robust against the asymmetric coupling [Figs. 4(e) and 4(h)]. The skin effect is quite obvious for second-order skin modes. As $\gamma = 0$, the bulk modes are mainly confined near the injected right port due to the propagation loss of the waveguide [Figs. 4(d)]. In contrast, for non-Hermitian cases, the bulk modes experiencing skin effects in both the x and y directions are driven to the

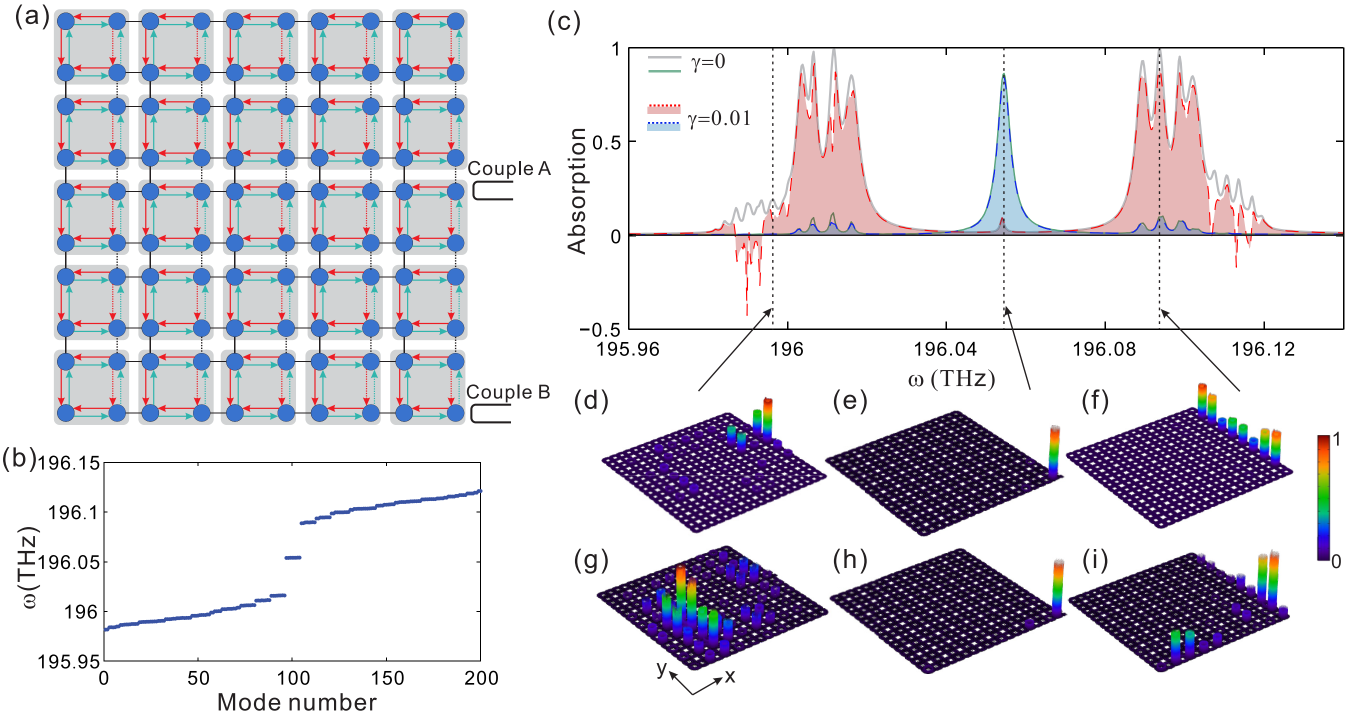

FIG. 4. The excitation of second-order topological, skin, and hybrid skin-topological modes in topological phase. (a) The schematic of the lattice and the position of excitation ports. (b) The spectrum of eigenfrequencies with $g_t = 0.35\,\mu\mathrm{m}$ and $g_\lambda = 0.26\,\mu\mathrm{m}$. (c) The absorption spectra using different external ports. (d–f) The spatial intensity profiles ($|\mathbf{E}|^2$) of bulk, corner, and edge modes for Hermitian cases at absorption peaks with $\omega = 195.996$, 196.055, 196.094 THz, indicated by the arrows. (g–i) The spatial intensity profiles of second-order skin, second-order topological, and hybrid skin-topological for non-Hermitian cases with $\gamma = 0.01$.

lower-left corner [Figs. 4(g)]. For hybrid skin-topological modes, they intrinsically undergo topological localization along one direction [Fig. 4(f)] and further are affected by the skin effect for nonvanished γ. As a result, they are accumu-

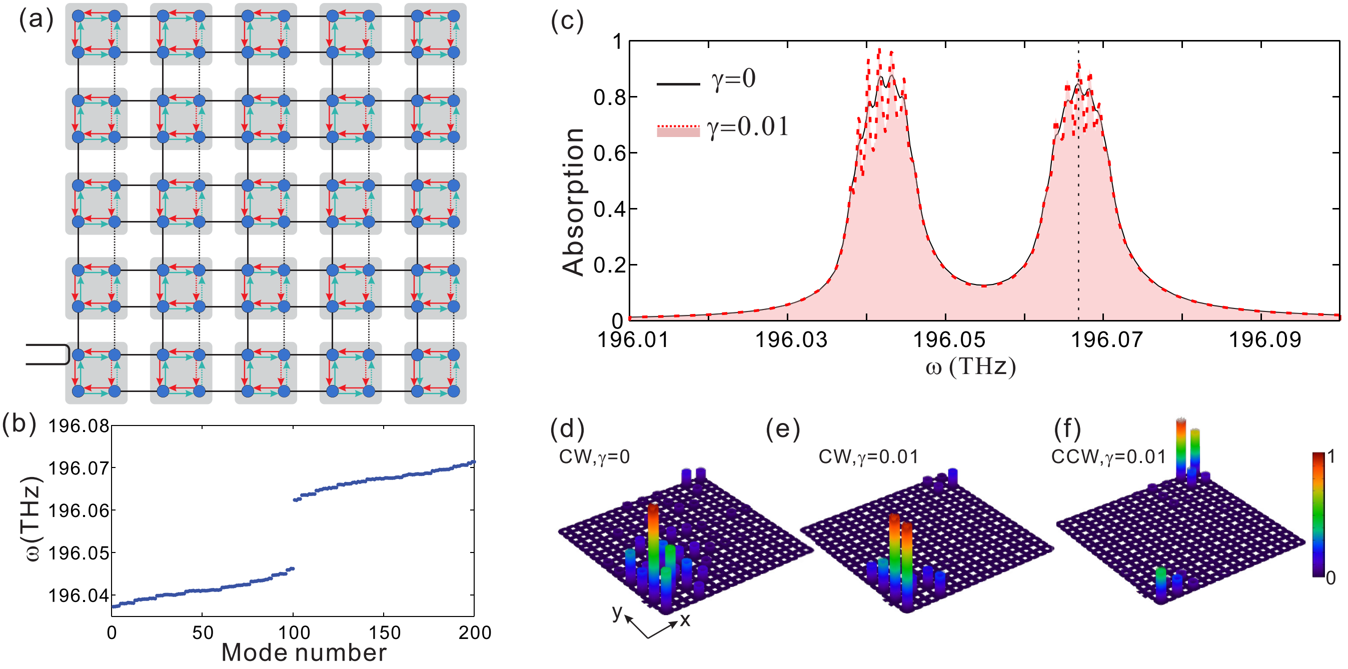

FIG. 5. The excitation of second-order skin modes in trivial phase. (a) The schematic of trivial lattice and the sketch of the excitation port. The gap between couplers and the arrays are $g_{\mathrm{in}} = 0.45$ and $0.35\,\mu\mathrm{m}$ for couplers A and B, respectively. (c) The absorption spectra for $\gamma = 0$ (black solid line) and $\gamma = 0.01$ (dotted line with pink area). (d, e) The spatial intensity profiles ($|\mathbf{E}|^2$) for clockwise modes as $\gamma = 0$ and $\gamma = 0.01$, respectively. (f) The intensity profile for counterclockwise modes as $\gamma = 0.01$. The intensity profiles are plotted at $\omega = 196.067$ THz. In all cases, $g_t = 0.35\,\mu\mathrm{m}$ and $g_\lambda = 0.40\,\mu\mathrm{m}$

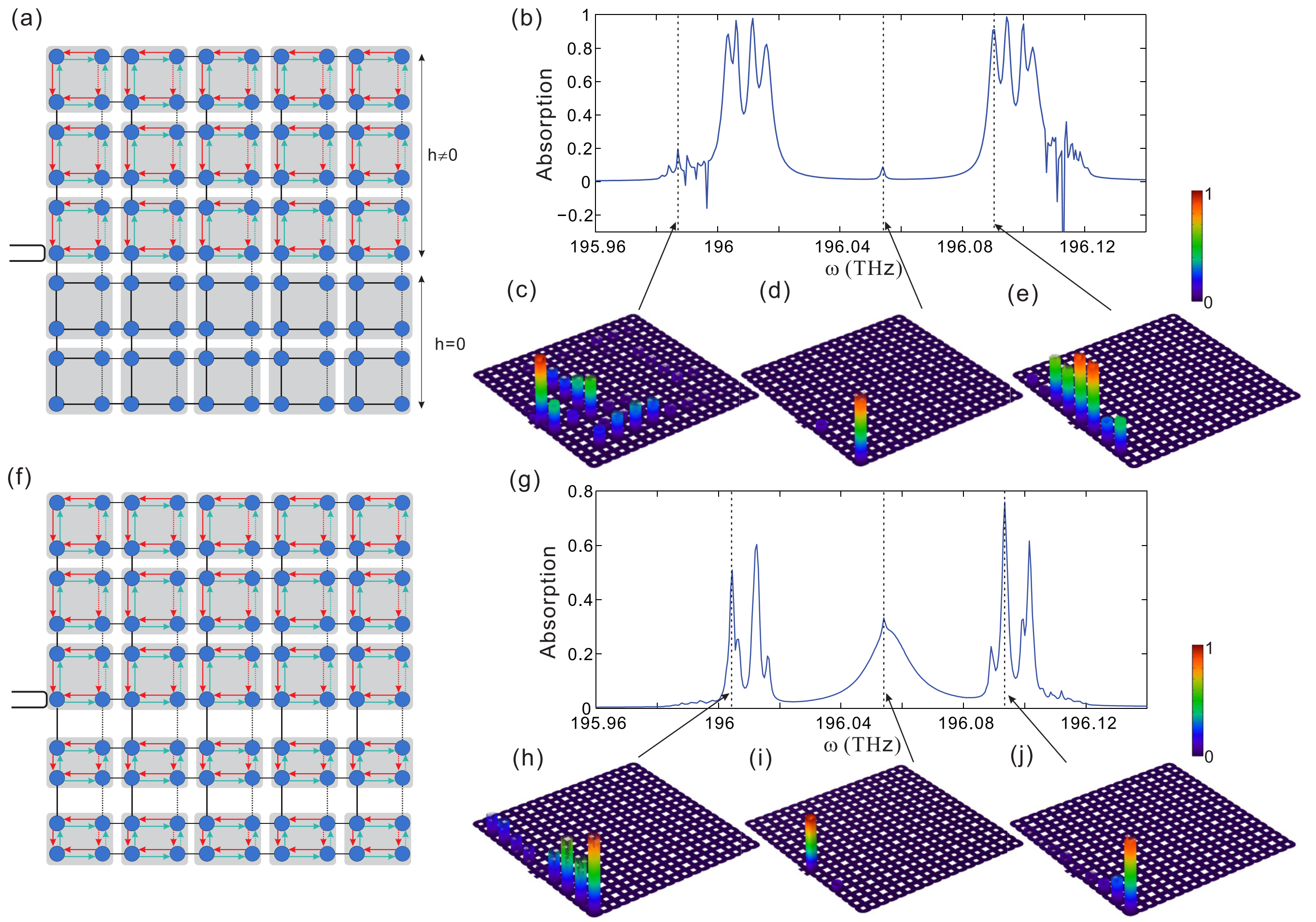

FIG. 6. Topological and skin modes at two different domain boundaries. (a) The schematic of the boundaries formed by imaginary gauge fields. (b)The absorption spectra corresponding to (a). (c, d) The spatial intensity profiles ($|\mathbf{E}|^2$) at $\omega = 195.987$, 196.054, and 196.091 THz. (f) Schematic of the lattice composed of topological and trivial systems. (g) The absorption spectra corresponding to (f). (h–j) The spatial intensity profiles ($|\mathbf{E}|^2$) at $\omega = 196.005$, 196.054, and 196.094 THz, indicated by the arrows in (g).

lated at the lower-right and lower-left corners [Fig. 4(i)]. In a Hermitian quadrupole insulator, the fields of second-order topological modes are distributed at all four corners, and the waves are accumulated at the corners near the injected port. This also applies to non-Hermitian cases with relatively small imaginary gauge fields. The electric fields are gradually concentrated on a single corner as h increases. This can be understood by the interplay of intrinsic localization of topological property and the skin effects caused by imaginary gauge fields. The skin effects drive light to the single corner for large h, which becomes more dominated when approaching trivial phases.

Next, we show the second-order skin effects retain in a trivial system in the absence of topological modes. Figure 5(a) shows the diagram of trivial lattice as $g_t = 0.35\,\mu$m and $g_\lambda = 0.40\,\mu$m, corresponding to a coupling strength of $t/\lambda \approx 2.4$. An external coupler is placed at the left edge. The simulated eigenfrequencies are plotted in Fig. 5(b), and there are no zero-energy modes in the bandgap. The absorption spectra for $\gamma = 0$ (black line) and $\gamma = 0.01$ (pink filling area) are shown in Fig. 5(c). The two spectra are similar, and both have two broadband absorption bands caused by bulk modes. Figures 5(d) and 5(e) show the field distributions for $\gamma = 0$ and 0.01 at frequency $\omega = 196.063$ THz. The modes spread into the bulk of the system for the Hermitian case. For a non-Hermitian case, light experiences strong localization at the lower-left corner due to the skin effects. Only a small part of energy is confined at upper right-corner, which is caused by the scattering in the structure. As discussed above, the clockwise and counterclockwise modes undergo opposite imaginary gauge fields and will concentrate at different corners. We launch light from the lower port of external coupler to stimulate counterclockwise modes. As shown in Fig. 5(f), light is confined at the upper-right corner.

The reasons for the formation of the topological and skin modes are different. The former is determined by the system topology and related to the relative coupling strengths, whereas the latter is determined by the imaginary gauge fields. Therefore, we can expect they will exhibit different behaviors at the interface of two different imaginary gauge fields and the interface of two topologically distinct structures. Figure 6(a) presents the effective lattice by connecting two structures with or without h. The corresponding absorption spectra are shown in Fig. 6(b). The position of absorption peaks is the same as that of Hermitian cases because the eigenfrequencies are irrelevant to the imaginary gauge field. The absorption in

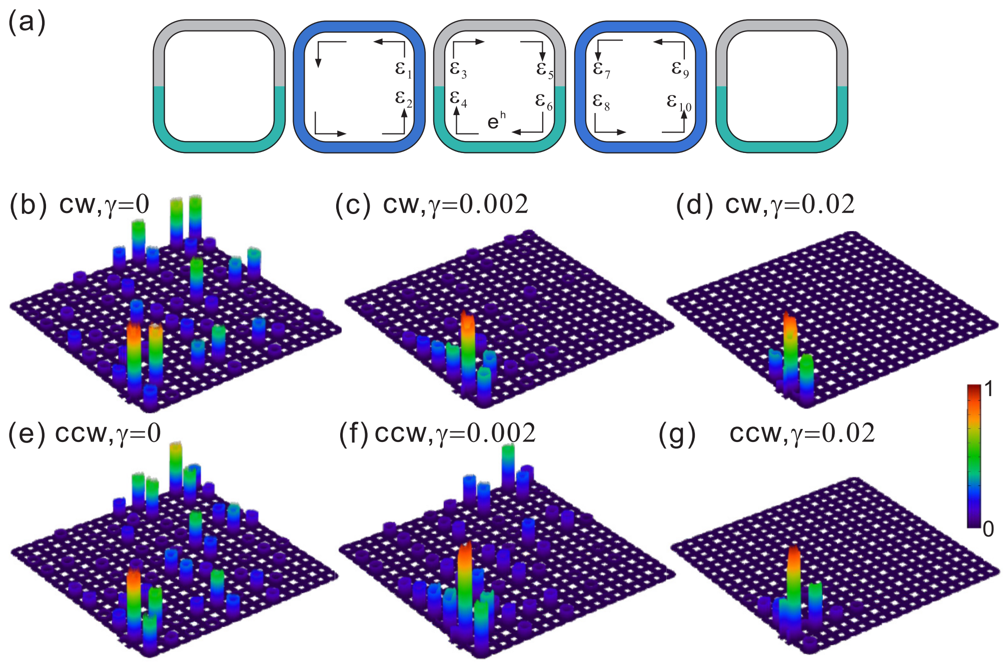

FIG. 7. Skin effects in passive resonator arrays. (a) The schematic of field amplitudes in coupled ring resonators. The spatial intensity profiles are for the clockwise excitation in (b)–(d) and are for the counterclockwise excitation (e)–(g). The incident frequency is $\omega = 196.11$ THz.

the middle band is lower compared to the sidebands as the incidence is weakly coupled to corner modes. For this configuration, the topological modes still appear in the lower-left corner and are not affected by the interface [Fig. 6(d)]. In contrast, the second-order skin modes in Fig. 6(c) are bound to the left side of the interface due to the skin effect in both dimensions. With similar localized properties to the second-order skin modes, the hybrid skin-topological modes gather at the interface [Fig. 6(e)], influenced by skin effect in y direction and topological localization in x direction. The situation becomes different as the domain boundaries are composed of the topological and trivial structures along the y direction, as displayed in Fig. 6(f). Figure 6(g) plots the corresponding absorption spectrum, which shows three absorption peaks. The spatial intensity distribution corresponding to the middle absorption peak around zero frequency detuning is confined at the middle corners, which is a combination of a topological boundary and a physical boundary [Fig. 6(i)]. Contrarily, as shown in Figs. 6(h) and 6(j), the hybrid modes in two sidebands penetrate though the interface and are accumulated at the lower-left corner of the physical boundary. The hybrid modes are immune to the topological boundary showing analogous features to the bulk modes in a one-dimensional system. In summary, the accumulation of second-order topological modes, skin modes, and hybrid skin-topological modes can be understood from the topological localization and the intrinsic skin effects in the x and y directions, as well as their interaction.

IV. THE PASSIVE RING RESONATORS

The imaginary gauge fields are induced by integrating asymmetric gain and loss into the two semicircles of the link rings. However, it is difficult to accurately keep them exactly equal in experiments. When their amount is different, we show the asymmetric coupling also can be be generated but with additional on-site gain or loss. Specifically, we discuss the passive cases with only loss inserted to the semicircle of link rings. For simplicity, a one-dimensional lattice is considered, as shown in Fig. 7(a). The fields between neighboring rings fulfill [14]

$$\begin{pmatrix}\varepsilon_5\\ \varepsilon_6\end{pmatrix}=\frac{1}{i\kappa}\begin{pmatrix}t & -1\\ 1 & -t\end{pmatrix}\begin{pmatrix}\varepsilon_3\\ \varepsilon_4\end{pmatrix}, \tag{11}$$

where t and κ denote the transmission and coupling coefficients with $t^2+\kappa^2=1$. Then the fields between two nearest site rings are derived as

$$\begin{aligned}\begin{pmatrix}\varepsilon_9\\ \varepsilon_{10}\end{pmatrix} &= \frac{1}{(i\kappa)^2}\begin{pmatrix}e^{-i\beta\frac{L_{SR}}{2}} & 0\\ 0 & e^{i\beta\frac{L_{SR}}{2}}\end{pmatrix}\begin{pmatrix}t & -1\\ 1 & -t\end{pmatrix}\\ &\quad\times\begin{pmatrix}e^{i\beta\frac{L_{LR}}{2}}e^{h} & 0\\ 0 & e^{-i\beta\frac{L_{LR}}{2}}\end{pmatrix}\begin{pmatrix}t & -1\\ 1 & -t\end{pmatrix}\begin{pmatrix}\varepsilon_1\\ \varepsilon_2\end{pmatrix}\\ &= M\begin{pmatrix}\varepsilon_1\\ \varepsilon_2\end{pmatrix},\end{aligned} \tag{12}$$

where L_{SR} and L_{LR} are the total length of site and link rings, and $\exp(h)$ indicates the decay times for light traveling through the lower path of the link rings. The Bloch theorem gives rise to $(\varepsilon_9, \varepsilon_{10})^T = \varepsilon^{i\varphi}(\varepsilon_1, \varepsilon_2)^T$. Combining with Eq. (12), solving equation $|M{-}e^{ik}I| = 0$ yields the dispersion relation. We also have $\beta L_{\mathrm{LR}}{-}\beta L_{\mathrm{SR}} = \pi + 2\,\mathrm{m}\pi$ or antiresonant condition. Then we arrive at

$$\begin{aligned}&2\sin\left(\beta L_{SR} + ih/2\right)\\ &\quad= it^2(e^{h/2} - e^{-h/2}) + \kappa^2 e^{h/2}e^{-ik} + \kappa^2 e^{-h/2}e^{ik}.\end{aligned} \tag{13}$$

In the vicinity of resonance, we can approximate $\sin(\beta L_{\mathrm{SR}} + ih/2) \approx (\omega - \omega_0)L_{SR}/v_g + ih/2$ with v_g denoting group velocity. The dispersion relation reduces to

$$\omega = \omega_0 + ith + t(e^{h/2}e^{-ik} + e^{-h/2}e^{ik}), \tag{14}$$

with $\tau = v_g k^2/(2L_{\mathrm{SR}})$. The imaginary gauge potential is the half of loss coefficient, and the on-site loss is *ith*. The results can be generated to a two-dimensional lattice, and the Hamiltonian of passive quadrupole insulator is

$$H = \begin{pmatrix} ith & & te^{-h/2} + \lambda e^{ik_x} & -te^{-h/2} - \lambda e^{ik_y} \\ & ith & te^{h/2} + \lambda e^{-ik_y} & te^{h/2} + \lambda e^{-ik_x} \\ te^{h/2} + \lambda e^{-ik_x} & te^{-h/2} + \lambda e^{ik_y} & ith & \\ -te^{h/2} - \lambda e^{-ik_y} & te^{-h/2} + \lambda e^{ik_x} & & ith \end{pmatrix}. \tag{15}$$

The skin effects also can be observed in the passive lattice. In Figs. 7(b)–7(g), we plot the intensity profiles for clockwise and counterclockwise excitation for three different γ. The wave is launched near the lower-left corner. The system is in topological trivial phase as the inter- and intracell gaps are $g_t = 0.35\,\mu$m and $g_l = 0.40\,\mu$m. For vanished γ, the fields are distributed through the structure because there are no skin effects, as shown in Figs. 7(b) and 7(e). We see the waves are localized at the lower-left corner for clockwise modes as $\gamma > 0$ [Figs. 7(c) and 7(d)]. For counterclockwise excitation, SS modes tend to be localized at the upper-right corner. As displayed in Fig. 7(f), there are some fields in the upper corner. However, the light is not able to spread to the upper-right corner due to the strong propagation loss for large γ [Fig. 7(g)]. To inspect the counterclockwise second-order skin mode, the incident port needs to be set in the upper-right corner.

V. CONCLUSIONS

In conclusion, we have proposed a non-Bloch quadrupole topological insulator with skin effects based on coupled ring resonator arrays. The π gauge flux and imaginary gauge fields are introduced by shifting and integrating asymmetric gain and loss into the auxiliary rings to induce a direction-dependent phase or amplification. The system simultaneously supports topological modes and skin modes, whose origins are different. The former is determined by the system topology and related to the couplings, whereas the latter is determined by the imaginary gauge potential. We show the emergency of the corner modes can be controlled by tuning the spatial gap distance between adjacent rings. The clockwise and counterclockwise modes experience opposite imaginary gauge fields. As a result, the skin modes are localized at the opposite corners depending on mode orientations. Moreover, we show the topological and skin modes can be localized at different boundaries by constructing topological or non-Hermitian interfaces, which can be understood by the interplay between topological localization and skin effects. We also show the imaginary gauge field can be introduced in passive ring resonators with additional on-site loss, and the skin effects are prominent only for single orientation modes. The results enrich the study of topological phases in non-Hermitian systems and promise potential applications in lasers and broadband light trapping.

ACKNOWLEDGMENT

The work is supported by the National Natural Science Foundation of China (NSFC) (11804259, 11974124).

[1] A. B. Khanikaev and G. Shvets, Two-dimensional topological photonics, Nat. Photon. **11**, 763 (2017).

[2] Z. Wang, Y. Chong, J. D. Joannopoulos, and M. Soljačić, Observation of unidirectional backscattering-immune topological electromagnetic states, Nature (London) **461**, 772 (2009).

[3] X. Han, K. Wang, P. D. Persaud, X. Xing, H. Long, F. Li, B. Wang, M. R. Singh, and P. Lu, Harmonic resonance enhanced second-harmonic generation in the monolayer WS_2-Ag nanocavity, ACS Photonics **7**, 562 (2020).

[4] W. Zhang, X. Chen, and F. Ye, Plasmonic topological insulators for topological nanophotonics, Opt. Lett. **42**, 4063 (2017).

[5] X. Han, K. Wang, X. Xing, M. Wang, and P. Lu, Rabi splitting in a plasmonic nanocavity coupled to a WS_2 monolayer at room temperature, ACS Photonics **5**, 3970 (2018).

[6] H. Ni, J. Wang, and A. Wu, Optical bistability in aperiodic multilayer composed of graphene and Thue-Morse lattices, Optik **242**, 167163 (2021).

[7] C. Shang, X. Chen, W. Luo, and F. Ye, Quantum anomalous Hall-quantum spin Hall effect in optical superlattices, Opt. Lett. **43**, 275 (2018).

[8] Z. Guo, J. Jiang, H. Jiang, J. Ren, and H. Chen, Observation of topological bound states in a double Su-Schrieffer-Heeger chain composed of split ring resonators, Phys. Rev. Res. **3**, 013122 (2021).

[9] L. Qi, G. Wang, S. Liu, S. Zhang, and H. Wang, Engineering the topological state transfer and topological beam splitter in an even-sized Su-Schrieffer-Heeger chain, Phys. Rev. A **102**, 022404 (2020).

[10] N. Fu, Z. Fu, H. Zhang, Q. Liao, D. Zhao, and S. Ke, Topological bound modes in optical waveguide arrays with alternating positive and negative couplings, Opt. Quant. Electron. **52**, 61 (2020).

[11] X. Cheng, C. Jouvaud, N. Xiang, S. H. Mousavi, A. Z. Genack, and A. B. Khanikaev, Robust reconfigurable electromagnetic

pathways within a photonic topological insulator, Nat. Mater. **15**, 542 (2016).

[12] J. W. Dong, X. D. Chen, H. Zhu, Y. Wang, and X. Zhang, Valley photonic crystals for control of spin and topology, Nat. Mater. **16**, 298 (2016).

[13] D. Leykam and L. Yuan, Topological phases in ring resonators: Recent progress and future prospects, Nanophotonics **9**, 4473 (2020).

[14] M. Hafezi, S. Mittal, J. Fan, A. Migdall, and J. M. Taylor, Imaging topological edge states in silicon photonics, Nat. Photon. **7**, 1001 (2013).

[15] L. Yuan, Y. Shi, and S. Fan, Photonic gauge potential in a system with a synthetic frequency dimension, Opt. Lett. **41**, 741 (2016).

[16] L. Yuan, M. Xiao, Q. Lin, and S. Fan, Synthetic space with arbitrary dimensions in a few rings undergoing dynamic modulation, Phys. Rev. B **97**, 104105 (2018).

[17] M. Hafezi, E. A. Demler, M. D. Lukin, and J. M. Taylor, Robust optical delay lines with topological protection, Nat. Phys. **7**, 907 (2011).

[18] F. Gao, Z. Gao, X. Shi, Z. Yang, X. Lin, H. Xu, J. D. Joannopoulos, M. Soljačić, H. Chen, L. Lu *et al.*, Probing topological protection using a designer surface plasmon structure, Nat. Commun. **7**, 11619 (2016).

[19] Y. G. Peng, C. Z. Qin, D. G. Zhao, Y. X. Shen, X. Y. Xu, M. Bao, H. Jia, and X. F. Zhu, Experimental demonstration of anomalous Floquet topological insulator for sound, Nat. Commun. **7**, 13368 (2016).

[20] Q. Lin, M. Xiao, L. Yuan, and S. Fan, Photonic Weyl point in a two-dimensional resonator lattice with a synthetic frequency dimension, Nat. Commun. **7**, 13731 (2016).

[21] W. A. Benalcazar, B. A. Bernevig, and T. L. Hqughes, Quantized electric multipole insulators, Science **357**, 61 (2017).

[22] W. Zhang, X. Xie, H. Hao, J. Dang, S. Xiao, S. Shi, H. Ni, Z. Niu, C. Wang, K. Jin, X. Zhang, and X. Xu, Low-threshold topological nanolasers based on the second-order corner state, Light. Sci. Appl. **9**, 109 (2020).

[23] G. Pelegri, A. M. Marques, V. Ahufinger, J. Mompart, and R. G. Dias, Second-order topological corner states with ultracold atoms carrying orbital angular momentum in optical lattices, Phys. Rev. B **100**, 205109 (2019).

[24] A. Dutt, M. Minkov, I. A. D. Williamson, and S. Fan, Higher-order topological insulators in synthetic dimensions, Light Sci. Appl. **9**, 131 (2020).

[25] Y. Chen, Z. K. Lin, H. Chen, and J. H. Jiang, Plasmon-polaritonic quadrupole topological insulators, Phys Rev. B **101**, 041109(R) (2020).

[26] S. Mittal, V. V. Orre, G. Zhu, M. A. Gorlach, A. Poddubny, and M. Hafezi, Photonic quadrupole topological phases, Nat. Photonics **13**, 692 (2019).

[27] Y. Ota, K. Takata, T. Ozawa, A. Amo, Z. Jia, B. Kante, M. Notomi, Y. Arakawa, and S. Iwamoto, Active topological photonics, Nanophotonics **9**, 547 (2020).

[28] Z. Fu, N. Fu, H. Zhang, Z. Wang, D. Zhao, and S. Ke, Extended SSH model in non-Hermitian waveguides with alternating real and imaginary couplings, Appl. Sci. **10**, 3425 (2020).

[29] H. Fan, J. Chen, Z. Zhao, J. Wen, and Y. Huang, Anti-parity-time symmetry in passive nanophotonics, ACS Photon. **7**, 3035 (2020).

[30] S. Ke, D. Zhao, Q. Liu, S. Wu, B. Wang, and P. Lu, Optical imaginary directional couplers, J. Lightwave Technol. **36**, 2510 (2018).

[31] Y. Ao, X. Hu, Y. You, C. Lu, Y. Fu, X. Wang, and Q. Gong, Topological Phase Transition in the Non-Hermitian Coupled Resonator Array, Phys. Rev. Lett. **125**, 013902 (2020).

[32] M. Parto, S. Wittek, H. Hodaei, G. Harari, M. A. Bandres, J. Ren, M. C. Rechtsman, M. Segev, D. N. Christodoulides, and M. Khajavikhan, Edge-Mode Lasing in 1D Topological Active Arrays, Phys. Rev. Lett. **120**, 113901 (2018).

[33] S. Malzard, C. Poli, and H. Schomerus, Topologically Protected Defect States in Open Photonic Systems with Non-Hermitian Charge-Conjugation and Parity-Time Symmetry, Phys. Rev. Lett. **115**, 200402 (2015).

[34] S. Ke, D. Zhao, J. Fu, Q. Liao, B. Wang, and P. Lu, Topological edge modes in non-Hermitian photonic Aharonov-Bohm cages, IEEE J. Sel. Top. Quantum Electron. **26**, 4401008 (2020).

[35] S. Yao and Z. Wang, Edge States and Topological Invariants of Non-Hermitian Systems, Phys. Rev. Lett. **121**, 086803 (2018).

[36] E. J. Bergholtz, J. C. Budich, and F. K. Kunst, Exceptional topology of non-Hermitian systems, Rev. Mod. Phys. **93**, 015005 (2021).

[37] C. Yuce, Non-Hermitian anomalous skin effect, Phys. Lett. A **384**, 126094 (2020).

[38] X. Wang, C. Guo, and S. Kou, Defective edge states and number-anomalous bulk-boundary correspondence in non-Hermitian topological systems, Phys. Rev. B **101**, 121116(R) (2020).

[39] N. Okuma, K. Kawabata, K. Shiozaki, and M. Sato, Topological Origin of Non-Hermitian Skin Effects, Phys. Rev. Lett. **124**, 086801 (2020).

[40] Y. He and C. C. Chien, Non-Hermitian generalizations of extended Su-Schrieffer-Heeger models, J. Phys. Condens. Matter. **33**, 085501 (2020).

[41] Z. Zhang, R. Huang, L. Qi, Y. Xing, Z. Zhang, and H. Wang, Topological phase transition and eigenstates localization in a generalized non-Hermitian Su–Schrieffer–Heeger model, Ann. Phys. **533**, 2000272 (2020).

[42] S. Mandal, R. Banerjee, and T. C. H. Liew, From the topological spin-Hall effect to the non-Hermitian skin effect in an elliptical micropillar chain, arXiv:2103.05480 (2021).

[43] W. X. Cui, L. Qi, Y. Xing, S. Liu, S. Zhang, and H. F. Wang, Localized photonic states and dynamic process in nonreciprocal coupled Su-Schrieffer-Heeger chain, Opt. Express **28**, 37026 (2020).

[44] K. Zhang, Z. S. Yang, and C. Fang, Correspondence between Winding Numbers and Skin Modes in Non-Hermitian Systems, Phys. Rev. Lett. **125**, 126402 (2020).

[45] L. Xiao, T. Deng, K. Wang, G. Zhu, Z. Wang, W. Yi, and P. Xue, Non-Hermitian bulk–boundary correspondence in quantum dynamics, Nat. Phys. **16**, 761 (2020).

[46] S. Weidemann, M. Kremer, T. Helbig, T. Hofmann, A. Stegmaier, M. Greiter, R. Thomale, and A. Szameit, Topological funneling of light, Science **368**, 311 (2020).

[47] T. Liu, Y. R. Zhang, Q. Ai, Z. Gong, K. Kawabata, M. Ueda, and F. Nori, Second-Order Topological Phases in Non-Hermitian Systems, Phys. Rev. Lett. **122**, 076801 (2019).

[48] Y. Song, W. Liu, L. Zheng, Y. Zhang, B. Wang, and P. Lu, Two-Dimensional Non-Hermitian Skin Effect in a Synthetic Photonic Lattice, Phys. Rev. Appl. **14**, 064076 (2020).

[49] K. Kawabata, M. Sato, and K. Shiozaki, Higher-order non-Hermitian skin effect, Phys. Rev. B **102**, 205118 (2020).

[50] C. H. Lee, L. Li, and J. Gong, Hybrid Higher-Order Skin-Topological Modes in Nonreciprocal Systems, Phys. Rev. Lett. **123**, 016805 (2019).

[51] Y. Tian X. Zhang, J. Jiang, M. Lu, and Y. Chen, Observation of higher-order non-Hermitian skin effect, arXiv:2102.09825 (2021).

[52] S. Longhi, D. Gatti, and G. Della Valle, Non-Hermitian transparency and one-way transport in low-dimensional lattices by an imaginary gauge field, Phys. Rev. B **92**, 094204 (2015).

[53] S. Longhi, D. Gatti, and G. Della Valle, Robust light transport in non-Hermitian photonic lattices, Sci. Rep. **5**, 13376 (2015).

[54] S. Longhi, Non-Hermitian gauged topological laser arrays, Ann. Phys. **530**, 1800023 (2018).

[55] X. Zhu, H. Wang, S. K. Gupta, H. Zhang, B. Xie, M. Lu, and Y. Chen, Photonic non-Hermitian skin effect and non-Bloch bulk-boundary correspondence, Phys. Rev. Res. **2**, 013280 (2020).

[56] L. Qi, G. Wang, S. Liu, S. Zhang, and H. Wang, Robust Interface-State Laser in Non-Hermitian Microresonator Arrays, Phys. Rev. Appl. **13**, 064016 (2020).

[57] Z. Lin, S. Ke, X. Zhu, and X. Li, Square-root non-Bloch topological insulators in non-Hermitian ring resonators, Opt. Express **29**, 8462 (2021).

[58] Z. Zhang, H. Zhao, D. G. Pires, X. Qiao, Z. Gao, J. M. Jornet, S. Longhi, N. M. Litchinitser, and L. Feng, Ultrafast control of fractional orbital angular momentum of microlaser emissions, Light. Sci. Appl. **9**, 179 (2020).

[59] K. Yokomizo and S. Murakami, Non-Bloch Band Theory of Non-Hermitian Systems, Phys. Rev. Lett. **123**, 066404 (2019).

[60] Y. Fu, J. Hu, and S. Wan, Non-Hermitian second-order skin and topological modes, Phys. Rev. B **103**, 045420 (2021).

[61] Y. Yu, M. Jung, and G. Shvets, Zero-energy corner states in a non-Hermitian quadrupole insulator, Phys. Rev. B **103**, L041102 (2021).